Diffusion entropy analysis in billiard systems

Gabriel I. Díaz,[1] Matheus S. Palmero,[1] Iberê Luiz Caldas,[1] and Edson D. Leonel[2]
[1]*Instituto de Física, IFUSP–Universidade de São Paulo, Rua do Matão, Cidade Universitária, 05314-970 São Paulo, SP, Brazil*
[2]*Departamento de Física, UNESP–Universidade Estadual Paulista, Bela Vista, 13506-900 Rio Claro, SP, Brazil*

(Received 26 August 2019; published 7 October 2019)

In this work we investigate how the behavior of the Shannon entropy can be used to measure the diffusion exponent of a set of initial conditions in two systems: (i) standard map and (ii) the oval billiard. We are interested in the diffusion near the main island in the phase space, where stickiness is observed. We calculate the diffusion exponent for many values of the nonlinear parameter of the standard map where the size and shape of the main island change as the parameter varies. We show that the changes of behavior in the diffusion exponent are related with the changes in the area of the main island and show that when the area of the main island is abruptly reduced, due to the destruction of invariant tori and, consequently, creation of hyperbolic and elliptic fixed points, the diffusion exponent grows.

DOI: 10.1103/PhysRevE.100.042207

I. INTRODUCTION

The diffusion problem in phase space for low-dimensional classical Hamiltonian systems is now very important from a theoretical point of view [1,2], where we care about the movement of an ensemble of noninteracting particles subjected to the dynamics described by the Hamiltonian. The presence of regular and chaotic trajectories produces different kinds of diffusion for densities of trajectories. Depending on the region in the phase space the diffusion may be normal or anomalous. The diffusion in phase space can be used in many problems as the study of Fermi acceleration [3–5], where the diffusion is along the energy axis or the study of transport properties from one region of phase space to another region [6,7].

Usually the diffusion is studied as the growth over time of the standard deviation of a generalized momentum variable [1,8–10]; in those studies it is considered that the diffusion along the generalized position, the anglelike variable, is fast. The growth over time of the standard deviation is characterized by two variables, a diffusion coefficient and a diffusion exponent, the most important being the exponent since it allows us to distinguish between anomalous diffusion, when the exponent is different from $1/2$, and normal diffusion, when the exponent is $1/2$. Even though this method gives good results in some cases, like in an almost completely chaotic sea [11,12], it fails in some other cases, since it is difficult to find the appropriate generalized momentum that it is better suited to describe a particular behavior in phase space [13,14], like around Kolmogorov-Arnold-Moser (KAM) islands [15–17].

A method that overcomes the standard-deviation problem was proposed by Scafetta and Grigolini [18] to characterize superdiffusive dynamics. We use their method, called diffusion entropy analysis (DEA), to study diffusion of trajectories with initial conditions around KAM islands, due the fact that the entropy is invariant under certain types of variable transformations, as changing from one set of canonical variables to another. Other problems, like the stickiness phenomena, can be addressed by this methodology.

It is known that stickiness plays an important role regarding transport properties in several areas of physics, such as fluids [19,20], plasma dynamics [21,22], and celestial mechanics [23]. For the generic KAM scenario strong fluctuations are observed due to the presence of Cantori [24] acting as a partial barrier to the transport of particles.

In this paper we use the DEA method to characterize the diffusion around KAM islands; we particularly focus in the subdiffusive behavior produced by the stickiness phenomena [25]. Thus we obtain a correlation between the diffusion exponent and geometry properties of the main island. In particular, we show that the diffusion exponent grows when the main island's area is abruptly reduced, due to the destruction of invariant tori and, consequently, creation of hyperbolic and elliptic fixed points.

The paper is organized as follows, Sec. II introduces the models under study, Sec. III describes the methodology used to find the diffusion exponent, in Sec. IV we show our numerical results, and, finally, conclusions are drawn in Sec. V.

II. THE MODELS

In this work we are interested in two different billiardlike models, such as the standard map (SM) and the oval billiard (OB). However, to illustrate the validation of the diffusion entropy analysis, the approach considered in this work, we are analyzing initially the simplified Fermi-Ulam model (SFUM), due to its phase-space properties.

The SFUM [4,26] consists of a classical particle suffering successive elastic collisions in a confined region bounded by two walls, separated by a distance equal to l, one of the walls is fixed and the other capable of exchange energy with the particle, affecting the particle's velocity depending on which phase of movement is the wall. The model has two unit dimensions, length and time, so we can choose that the distance between the walls and the angular frequency of the walls' phase change are equal to 1. The system is described by a two-dimensional nonlinear map $T_{\mathrm{SFUM}}(\phi_n, V_n) = (\phi_{n+1}, V_{n+1})$,

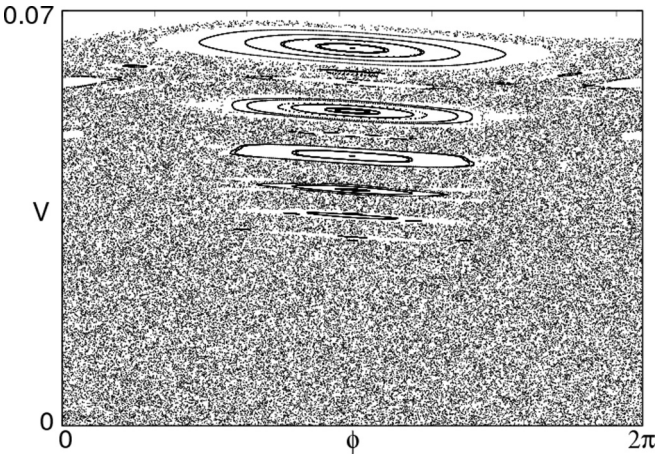

FIG. 1. Phase-space portrait of simplified Fermi-Ulam model for $\varepsilon = 0, 001$.

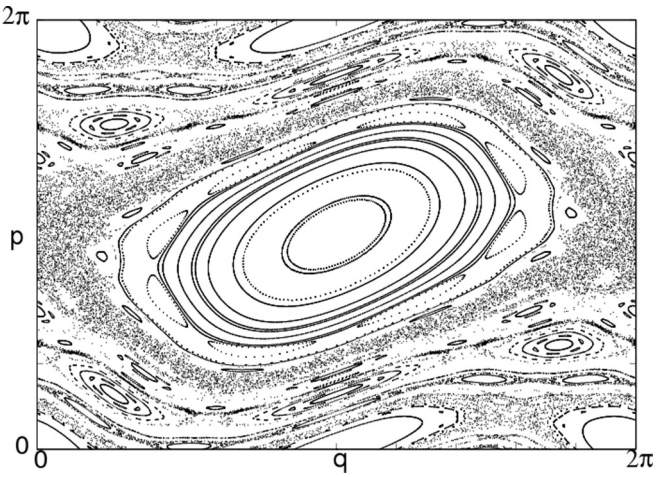

FIG. 2. Phase-space portrait of standard map for $k = 1$.

where V_n represents the particles velocity after the nth collision with the moving wall and ϕ_n is the phase of movement of the wall at the collision moment. The mapping that allows us to calculate the velocity and phase of the $(n+1)$th collision is given by

$$T_{\mathrm{SFUM}} : \begin{cases} \phi_{n+1} = \left[\phi_n + \frac{2}{V_n}\right] \mod (2\pi) \\ V_{n+1} = \|V_n - 2\varepsilon \sin(\phi_{n+1})\| \end{cases} . \tag{1}$$

The term $\frac{2}{V_n}$ corresponds to the time between collisions and $-2\varepsilon \sin(\phi_{n+1})$ gives the gain or loss of velocity or energy in each collision. The absolute value in the velocity is to reinject the particle in the correct direction after each collision, i.e., toward the fixed wall. Although this map is not written in *position-momentum* variables, it is area preserving. We can check this statement by taking the determinant of the Jacobian of $T_{\mathrm{SFUM}}(\phi_n, V_n) = (\phi_{n+1}, V_{n+1})$ and seeing that the absolute value always equals 1.

The characteristic phase space of the SFUM is composed of a large chaotic sea for low-velocity values, and then, as velocity grows, some KAM islands appear due to correlations between the velocity and the phase. Figure 1 shows the SFUM phase space.

The SFUM phase space is suitable to refine the method that we are going to describe in the next section. It is known that an ensemble of trajectories with initial small velocity must diffuse with exponent $1/2$ [11,12], and this is helpful to define the best grid divisions for other systems, which is very important to our approach.

On one hand, the standard map [27,28], describes the motion of a particle constrained to move in a ring. The particle is kicked periodically by an external field. This particular system is equivalent to a freely moving particle in a one-dimensional linear billiard, whose size is 2π, the particle suffers elastic collisions at the boundary, and the kicks are an external force changing the particle's movement. The standard map is described by the Hamiltonian

$$H(q, p, t) = \frac{p^2}{2mr^2} + K\cos(q)\sum_{n=-\infty}^{\infty}\delta(t/T - n), \tag{2}$$

where δ is the Dirac δ function, q is the angular coordinate, and p is its conjugate momentum. It is worth noting that we can consider that the particle's mass m, the ring's radius r, and the period of kicks T are equal to 1; this due the fact that we have three unit dimensions, length, time, and energy (or mass). The mapping $T_{\mathrm{SM}}(p_n, q_n) = (p_{n+1}, q_{n+1})$ that gives the position and momentum just before the $(n+1)$th collision is

$$T_{\mathrm{SM}} : \begin{cases} p_{n+1} = [p_n + k\sin(q_n)] \mod (2\pi) \\ q_{n+1} = [q_n + p_{n+1}] \mod (2\pi) \end{cases} , \tag{3}$$

where the parameter k controls the intensity of the nonlinearity of the mapping. This is also an area-preserving map. A portrait of the phase space of SM is shown in Fig. 2.

For this value of parameter, $k = 1$, there is coexistence of dynamics, chaotic trajectories around regular ones, and the regions of regular motion are generally formed by invariant curves arranged in complex structures called KAM islands [15–17,25].

In the other hand, the oval billiard, introduced M. Berry in Ref. [29], is now a well-studied billiard system. The radius of the boundary, in polar coordinates, is given by

$$R(\theta, \varepsilon, p) = 1 + \varepsilon\cos(p\theta). \tag{4}$$

The parameter $\varepsilon \in [0, 1)$ controls the deformation of the circle, the nonlinearity, p, is an integer number, and $\theta \in [0, 2\pi)$ is the polar angle.

After each collision of the particle with the wall we write two variables, the angle θ of collision and the angle α, which makes the trajectory with the tangent to the boundary. We consider elastic collisions so the velocity component tangent to the boundary is conserved while the normal component changes sign. Between collisions the particle moves in straight lines, *free-moving particle*s, see the trajectories in red in Fig. 3.

If we know the position (x_n, y_n) and velocity (v_{x_n}, v_{y_n}) of the particle immediately after a collision, iteration n, then we want to know the position (x_{n+1}, y_{n+1}) and the velocity $(v_{x_{n+1}}, v_{y_{n+1}})$ of the particle after the next collision, iteration $n+1$.

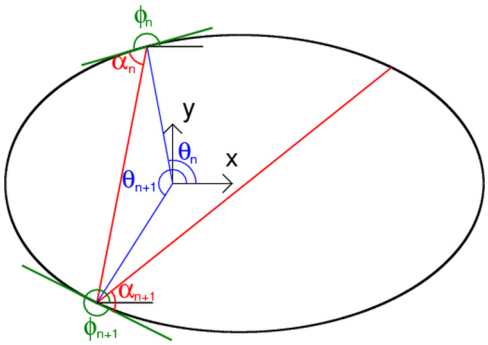

FIG. 3. Trajectory of a particle inside an oval billiard with $p = 1$ and $\varepsilon = 0.3$.

For the case of $p = 1$ a procedure exists to find the exact solution: Rewrite the boundary radius in the following way:

$$R_b = 1 + \varepsilon \frac{x_{n+1}}{R_b}, \tag{5}$$

where R_b is the radius of the boundary in collision $n + 1$.

Since the particle moves freely between collisions we know that $x_{n+1} = x_n + v_{x_n} t$, t is the time from collision n to collision $n + 1$. After some algebra with Eq. (5) we arrive at

$$R_b^2 = \left[R_b^2 - \varepsilon(x_n + v_{x_n} t)\right]^2. \tag{6}$$

Then we use the following auxiliary variables: $A = x_n^2 + y_n^2$, $B = 2(x_n v_{x_n} + y_n v_{y_n})$, and $C = v_{x_n}^2 + v_{y_n}^2$ and the fact that $R_b^2 = (x_n^2 + v_{x_n} t)^2 + (y_n^2 + v_{y_n} t)^2$ in Eq. (6) to find

$$\begin{aligned} &\left(-A + A^2 - 2A\varepsilon x_n + \varepsilon^2 x_n^2\right) \\ &\quad + \left(-B + 2AB - 2B\varepsilon x_n - 2\varepsilon A v_{x_n} + 2\varepsilon^2 x_n v_{x_n}\right) t \\ &\quad + \left(B^2 - C + 2AC - 2C\varepsilon x_n + \varepsilon^2 v_{x_n} - 2\varepsilon B v_{x_n}\right) t^2 \\ &\quad + \left(2BC - 2\varepsilon C v_{x_n}\right) t^3 + C t^4 = 0. \end{aligned} \tag{7}$$

The first term is zero since the initial position is in the boundary, and then we have to solve a third-degree polynomial, which has an exact solution [30]. We use the algorithm written by Skowron and Gould [31] to find the roots of the polynomial, and then we choose the smallest real root bigger than zero; this is our time between collision n and $n + 1$. With this we can find the collision angle θ_{n+1}. We note that similar procedures can be done for different values of p, although for $p > 2$ the polynomial degree is 5 or more so approximated solutions must be found.

We are interested now in the angle α_{n+1}, and by means of Fig. 3 we find the relation

$$\alpha_{n+1} = \phi_{n+1} - (\alpha_n + \phi_n), \tag{8}$$

where the auxiliary angle ϕ is related to the tangent line to the boundary at the point of collision. Namely ϕ is the angle between the x axis and the tangent line, so it is given by

$$\phi = \arctan\left(\frac{dY_b}{dX_b}\right). \tag{9}$$

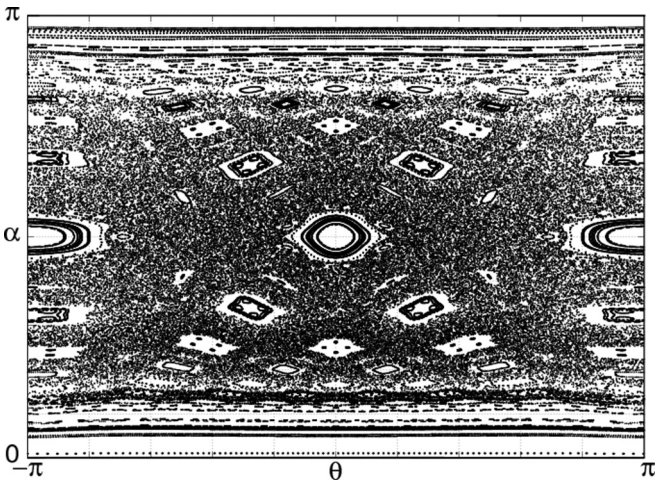

FIG. 4. Phase-space portrait of oval billiard for $\varepsilon = 0.3$.

Using the chain rule and the parametric description of the boundary given by θ, we finally find that ϕ is

$$\phi_n = \arctan\left[\frac{-p\varepsilon \sin(p\theta_n)\sin(\theta_n) + R(\theta_n)\cos(\theta_n)}{-p\varepsilon \sin(p\theta_n)\cos(\theta_n) - R(\theta_n)\sin(\theta_n)}\right]. \tag{10}$$

The mapping $T_{\mathrm{OB}'}(\theta_n, \alpha_n) = (\theta_{n+1}, \alpha_{n+1})$ is not area preserving, and we have to transform to Poincaré-Birkhoff coordinates [32] to have an area-preserving map; these are given by the arc-length, s_n, and the tangential velocity, v_n, to the collision point.

The tangential velocity, v_n, in the nth collision is given by

$$v_{n+1} = \cos(\alpha_{n+1}). \tag{11}$$

The arc-length, s_n, at the nth iteration can be found by the integral

$$s_n = \int_0^{\theta_n} \sqrt{R(\theta)^2 + \left[\frac{dR(\theta)}{d\theta}\right]^2}\, d\theta, \tag{12}$$

where the radius $R(\theta)$ is parametrized by the angle θ, Eq. (4). Considering $p = 1$ and after some algebra we arrive at

$$s_n = \frac{2}{1+\varepsilon} \int_0^{\frac{\theta_n}{2}} \sqrt{1 - \frac{4\varepsilon}{(1+\varepsilon)^2}\sin^2(u)}\, du, \tag{13}$$

which can be written in terms of the incomplete elliptic integral of second type $E(\theta, k)$ [33]

$$E(\theta, k) = \int_0^{\theta} \sqrt{1 - k^2 \sin^2(u)}\, du, \tag{14}$$

the numerical value can be computed efficiently using the subroutines provided in Ref. [34]. The new mapping $T_{\mathrm{OB}}(s_n, v_n) = (s_{n+1}, v_{n+1})$ is given by

$$T_{\mathrm{OB}} : \begin{cases} s_{n+1} = \frac{2}{1+\varepsilon} E\left(\frac{\theta_{n+1}}{2}, \frac{2\sqrt{\varepsilon}}{1+\varepsilon}\right) \\ v_{n+1} = \cos(\alpha_{n+1}) \end{cases}. \tag{15}$$

The characteristic phase space of the OB is shown in Fig. 4. Analogously to the phase space of the SM, depicted in Fig. 2, the phase space of the OB is composed of a chaotic sea and KAM islands. Considering different values of the parameter ε, geometric properties of the main islands, such area and

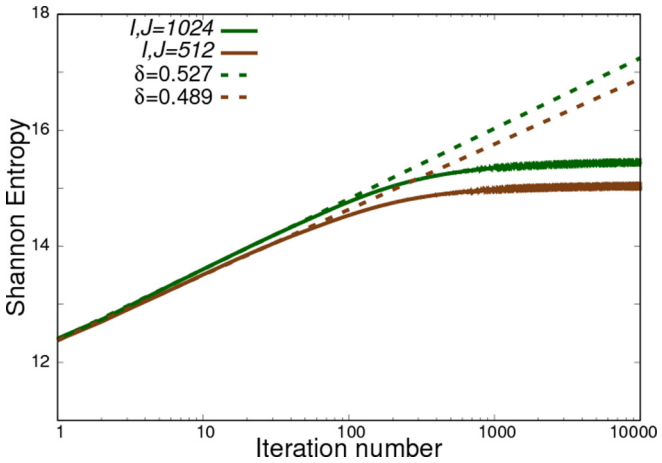

FIG. 5. Plot of the entropy vs. iteration number for different number of grid divisions. We use the simplified Fermi-Ulam model with parameter $\epsilon = 0.001$. We also show the value of δ in the diffusive regime, i.e., logarithmic growth of the entropy.

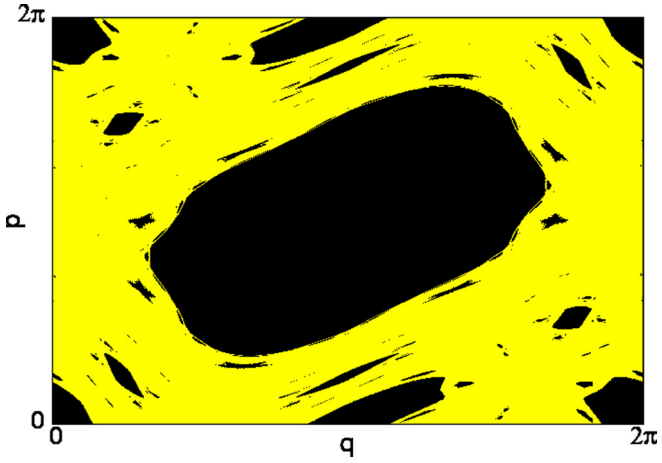

FIG. 6. Separation the sea of chaos (yellow) from the regular islands (black) in the standard mapping for $k = 1.31$.

perimeter, may suffer important changes that can be related to transitions in the diffusion and transport properties for the phase space.

III. THE METHOD

In order to calculate the diffusion exponent, Scafetta and Grigolini proposed to study the growth of entropy over time [18]. Assuming a scaling behavior for the probability density function, $\rho(x, n)$, it was proven that the Shannon entropy, $S = -\int_{-\infty}^{\infty} \rho(x, n) \ln [\rho(x, n)] dx$, had the following relation with time:

$$S = A + \delta \ln (n), \tag{16}$$

where they define δ as the diffusion exponent, n is the iteration number, i.e., the time, and A is a constant with no importance for our present analysis. In our numerical experiments we measure the Shannon entropy in the following way: (i) Choose a regular two-dimensional grid with I (horizontal divisions) $\times J$ (vertical divisions). (ii) Choose an ensemble of initial conditions to apply the mapping. (iii) After each iteration of the given mapping, we count how many points are inside each box of the grid, and with this information we construct a histogram $[h_{ij}]$. The Shannon entropy [35] is numerically given by:

$$S = -\sum_{i=1}^{I} \sum_{j=1}^{J} h_{ij} \ln(h_{ij}), \tag{17}$$

where the sum of all the elements of the histogram $[h_{ij}]$ is 1 [36]. To use Eq. (16) and Eq. (17) is important to use area-preserving maps; otherwise, additional terms must be considered to account for different box weights that change from one position to another.

We use the SFUM. Eq. (1), as a first example to refine the method. For this case we know that an ensemble of trajectories with initial small velocity must diffuse with exponent 1/2 [11,12], and we perform numerical experiments with different grid divisions $I \times J$, shown in Fig. 5, to understand how to choose the number of boxes.

In Fig. 5 we show the entropy behavior over time and the diffusion exponent for the diffusive regime with different number of boxes. Changing the number of divisions $I \times J$ in the grid gives different behavior of entropy over time. We also show the value of the diffusion exponent δ after performing a fit with function $S = A + \delta \ln (n)$ in the diffusive regime, i.e., where there is a logarithmic growth of the entropy. A final plateau is reached by each entropy curve; this corresponds to an ensemble of conditions uniformly distributed in the chaotic region.

From Refs. [11,12] we know that the diffusion exponent δ must be near 0.5 for this numerical experiment. Even more, from Ref. [12], we know that the standard deviation of the fluctuations is $\sqrt{2}\epsilon$, and from Ref. [11] we know that the diffusion range goes from $V_{\min} = 0$ to $V_{\max} = 2\sqrt{\epsilon}$. The division $\frac{2\sqrt{\epsilon}}{\sqrt{2}\epsilon}$, i.e., *diffusion range* over *fluctuation size*, gives the value 44.72, we observe that this number is one order less than the I, J value that gives the best approximation to the diffusion exponent in Fig. 5. From this observation we arrive to the following empirical relation:

$$10 \times \frac{\text{diffusion range}}{\text{fluctuation size}} \sim \text{grid divisions}. \tag{18}$$

Having the empirical relation (18) we proceed to study the diffusion behavior near the KAM islands, first we care about the SM, Eq. (3). To get near the main island we use the following procedure. We know that there is a hyperbolic fixed point at coordinates $q = 0$, $p = \pi$ in a chaotic region. Choosing many initial conditions in this region we know that they will expand all over the chaotic sea after many iterations of the mapping. Then we separate the regions visited by the points and the regions that were not visited, see Fig. 6, where we divided the phase space in a grid of 4096×4096. We choose 1×10^7 initial conditions near the point $[0, \pi]$. For each initial condition we discarded the first 1×10^3 iterations of the map to give time to the points to get near the islands. Then we iterated 1×10^7 times the mapping, and if any of the points were inside a box of our grid, we assigned the yellow

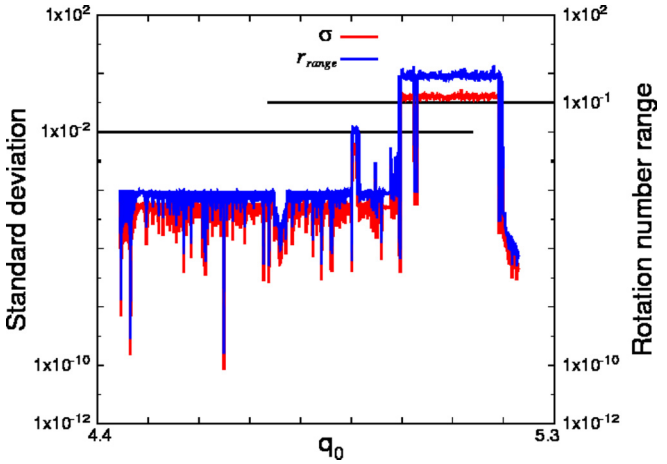

FIG. 7. The horizontal axis gives the orbit initial coordinate q_0, while p_0 is always π. For each initial condition we calculate the rotation number 1000 times at intervals of 1000 iterations and analyze its distribution. The vertical axis shows the standard deviation σ and rotation number range r_{range} of those distributions; we also show the horizontal cuts $\sigma = 1 \times 10^{-2}$ and $r_{\text{range}} = 1 \times 10^{-1}$. The model under study is the standard map with $k = 1.31$.

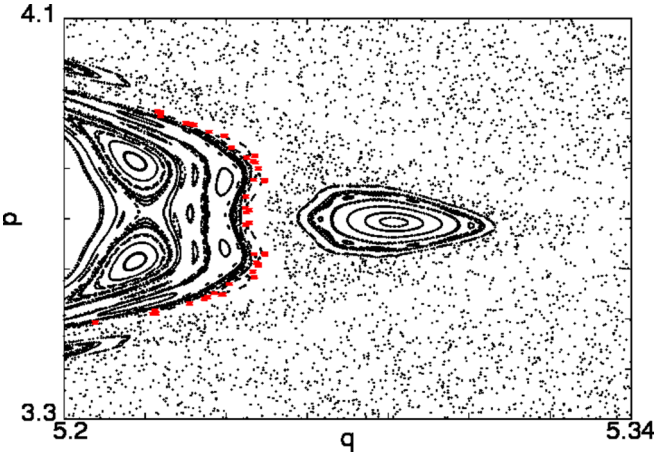

FIG. 8. Phase-space portrait of the standard map for $k = 1.31$. The red points are the initial coordinates that will spread in phase space and will be used to calculate the diffusion exponent.

color for that box; if after all iterations no point happened to be inside a box, then it was assigned the black color. In this way we had an approximation of the chaotic sea and islands in the given grid.

The main island's center is an elliptic fixed point of coordinates $q = \pi$, $p = \pi$. It is inside a black box in Fig. 6. Selecting all the black boxes that are connected, i.e., that are first nearest neighbors, starting from that one, we are able to find an approximation of the main island area by a black region of simple connected boxes. An approximation of the main island's area is given by dividing the number of black boxes that compound this region by 4096×4096 and multiplying by $(2\pi)^2$.

To get closer to the main island we investigate the rotation number. We consider the center of the island as our reference point and the ray $q > \pi$, $p = \pi$ as our polar axis and calculate, after each iteration n, the angle θ_n that an orbit has with the polar axis. The rotation number is defined as:

$$r = \lim_{N\to\infty} \frac{\sum_{n=0}^{N} \theta_n}{N}. \tag{19}$$

In practice we choose $N = 1000$, but we analyze the statistical behavior of 1000 rotations numbers calculated for the same orbit at different times; if this is a quasiperiodic orbit, then these rotation numbers must be almost equal, and we expect that for a single quasiperiodic orbit these rotation numbers have a Gaussian distribution with small standard deviation, σ, and small range between the maximal and the minimal rotation numbers found for the same orbit, r_{range}. On the other hand, if the orbit is chaotic, then we expect the standard deviation and the range to be big. To find the shore of the main island, first we take the coordinate q_i of the first yellow box that has $q > \pi$ and $p = \pi$ in Fig. 6. Then we choose initial conditions with $p_0 = \pi$ and different values of q_0 around q_i, and we take care that the minimal q_0 is actually inside the island; this will be of use later. For each of these initial conditions we analyze the rotation number statistics as described in the last paragraph.

In Fig. 7 we show the rotation number statistical behavior for different initial conditions. The horizontal axis gives the orbit initial q_0 coordinate, p_0 is always π, and the vertical axis shows the standard deviation and the range between the maximal and the minimal rotation numbers. To separate quasiperiodic and chaotic behaviors we perform the cuts in $\sigma = 1 \times 10^{-2}$ and $r_{\text{range}} = 1 \times 10^{-1}$, meaning that any orbit that has both statistical measures above the cuts is considered chaotic; otherwise, it is considered quasiperiodic. From these results we care about the chaotic orbit that has the minimum q_0 for the interval considered, and we call this value q_{0c} [37]. Once we have this coordinate we save the first 1000 iterations of the map starting from the point $[q_{0c}, \pi]$, and

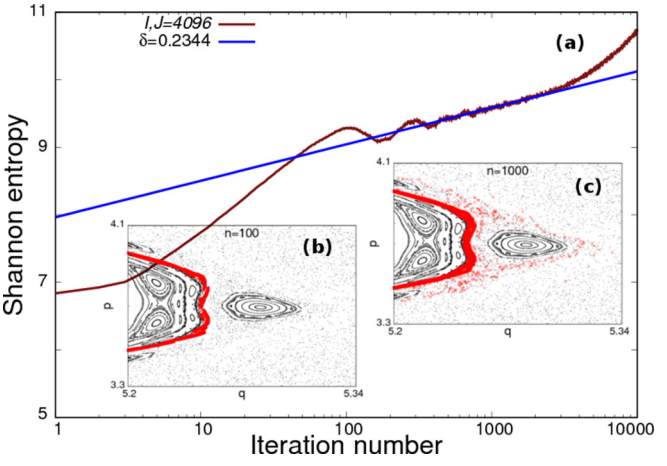

FIG. 9. Plot of the entropy vs. iteration number for $k = 1.31$. The entropy has three growth regimes: (i) In the first 100 iterations the distribution spreads along the main island, (ii) then for 3000 iterations slowly leaks out through the Cantori, and (iii) finally more of the distribution is outside the Cantori and rapidly spreads in the chaotic sea.

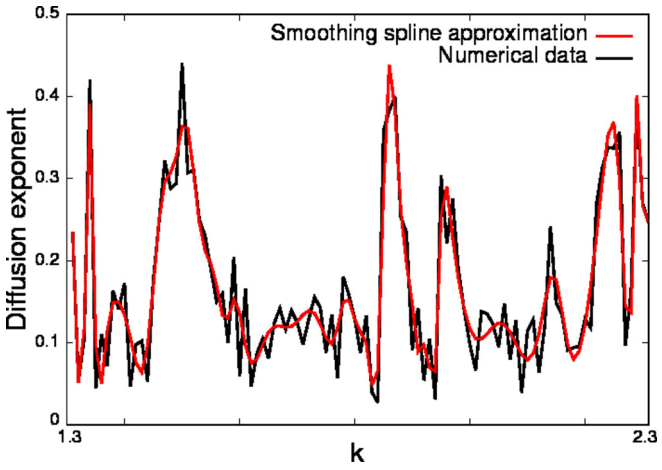

FIG. 10. Plot of the diffusion exponent vs. parameter k of standard map. The black line represents the numerical data obtained after the power-law fitting and the red line is a quintic spline smoothing approximation to the numerical data.

then we add an small perturbation to each one of those 1000 iterations until we have an array of 1×10^6 points. This array of coordinates will be our initial conditions that approach our initial distribution ρ_0, they will spread in the phase space, and we will use them to calculate the diffusion exponent by means of Eq. (16) and Eq. (17), see Fig. 8.

The next step to be taken before being able to measure the diffusion exponent is to define the grid box size. For this, we make use of the relation (18). We know that the *diffusion range* is 2π for both q and p. To estimate the value of *fluctuation size* we need to know how much our initial distribution, ρ_0, spreads with few mapping iterations, and this can be done in the following way: (i) Perform a map iteration on our initial conditions. Even if the ith point jumps

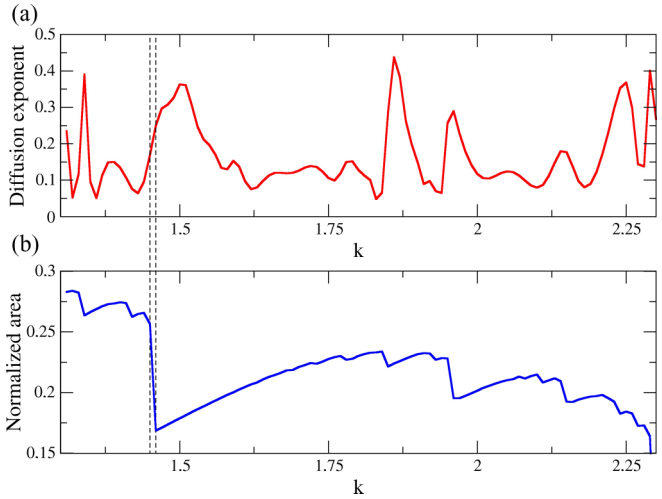

FIG. 11. In (a) and (b) we show, respectively, the plot of the diffusion exponent (red line) and the plot of the normalized area of the main island (blue line) vs. parameter k of the standard map. The normalized area is the area of the main island divided by the the area of the entire phase space. The region between dashed lines corresponds to the interval $k \in [1.45, 1.46]$.

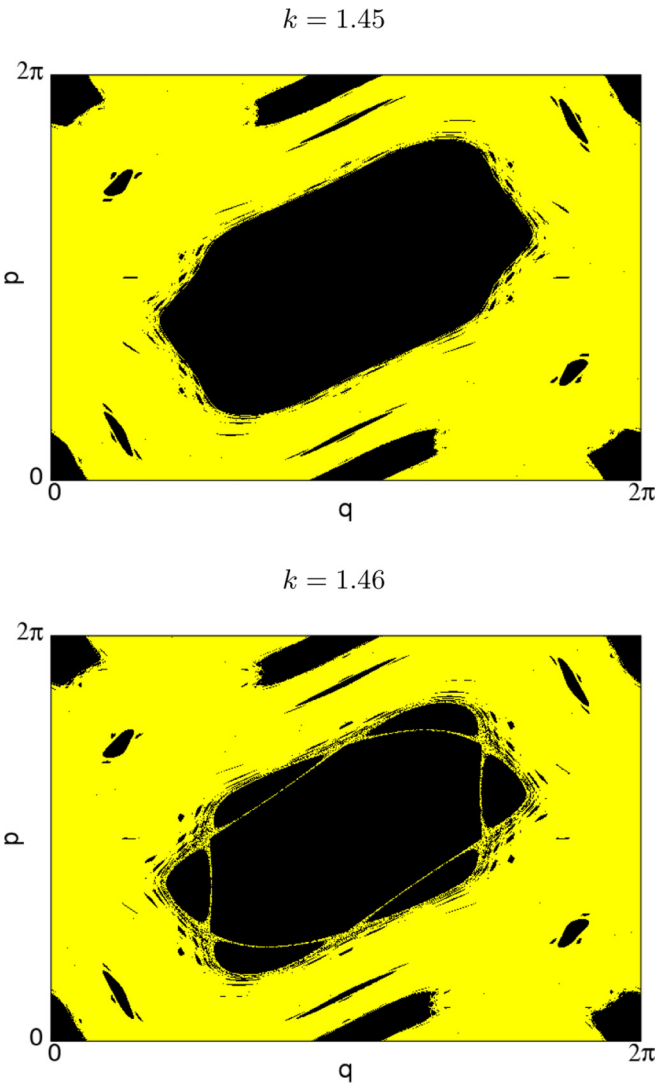

FIG. 12. Separation in the sea of chaos (yellow) from the regular islands (black) in the standard mapping for two values of the nonlinear parameter. Smaller islands are ejected from the main island when we change the parameter value. Associated to this islands are hyperbolic fixed points, and by the action of their stable and unstable manifolds they provide channels to escape from the main island; this yield to growth in the diffusion exponent.

far away from its starting position after one iteration, say, $x_{i,n} \to x_{i,n+1}$, some other point, say, the jth, will land near the starting position of the ith point, $x_{j,n+1} \sim x_{i,n}$. (ii) For each one of our initial points $[x_{i,n=0}]$ we search for the $x_{j,n=1}$ points such that $x_{j,n=1} \sim x_{i,n=0}$. (iii) Define the fluctuation at the $n = 1$ iteration as $\xi_{i,n=1} = x_{j,n=1} - x_{i,n=0}$; we do the same for more iterations, 10 iterations in our case. (iv) After that we can approximate the *fluctuation size* as the standard deviation of the $[\xi_{i,n}]$ fluctuations. Observe that this approximation is valid for orbits that are near the main island as our initial distribution is around its shore. In this case we find that $10 \times \frac{\text{diffusion range}}{\text{fluctuation size}} = 4856.2$, thus our space must be divided into 4096×4096 boxes of equal size, and with this grid choice we calculate the diffusion exponent.

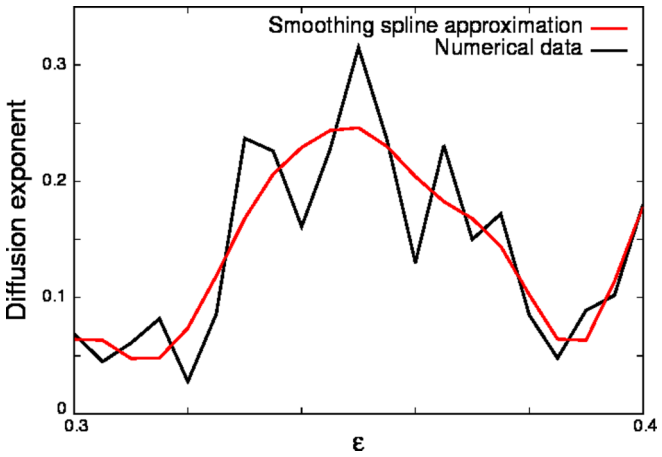

FIG. 13. Plot of the diffusion exponent vs. parameter ε of an oval billiard. The black line represents the numerical data obtained after the power-law fitting and the red line is an quintic spline smoothing approximation to the numerical data.

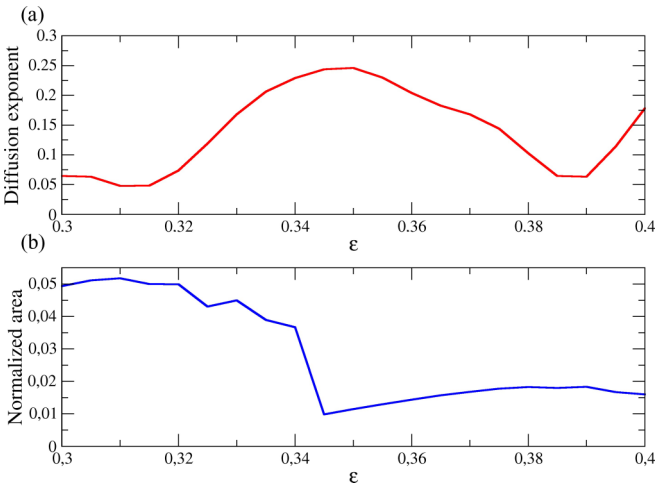

FIG. 14. In (a) and (b) we show, respectively, the plot of the diffusion exponent (red line) and normalized area of the main island (blue line) vs. parameter ε of an oval billiard.

We show in Fig. 9(a) the entropy behavior as time passes. We can recognize three growth regimes: (i) First, the distribution quickly spreads along the shore of the main island. We can appreciate this in Fig. 9(b), which shows in red how our ensemble of trajectories is distributed after $n = 100$ iterations. (ii) The second regime is a slow one; the distribution leaks through the Cantori, see Fig. 9(c). This is a regime of subdiffusion, one where we measure the diffusion exponent, and the numerical fit is shown with a blue line and the value of δ is 0.2344. (iii) In the third regime more of the distribution is outside the Cantori and rapidly spreads in the chaotic sea. A fourth regime, not shown in Fig. 9, exists, where the ensemble of trajectories is uniformly distributed in the chaotic sea, and, similarly as in Fig. 5, the entropy reaches a plateau.

IV. NUMERICAL RESULTS

Considering initially the standard map to understand how δ depends on the control parameter, we measure the diffusion exponent for 101 different values of the parameter equally spaced from $k = 1.31$ to $k = 2.31$. In Fig. 10 we see the behavior of the diffusion exponent when the parameter k changes. Since this behavior is very noisy, in part due the election of initial probability distribution, we perform a quintic spline smoothing approximation to the data [38]. This allows us to see easily the tendency of the data, i.e., the growth and decay of δ. Next we will shall relate the diffusion exponent to some geometric property of the main island, and we choose to measure the area of it for all the given values of k.

It is possible to see in Fig. 11 that whenever the area decreases abruptly the diffusion exponent increases. Furthermore the area grows, while the exponent decreases, until a critical value when the area abruptly decreases once more, with its corresponding increase in the diffusion exponent. We note two values of k, the region between the dashed lines in Fig. 11. In this interval the largest decrease in the area is shown for the values of k considered.

We see in Fig. 12 the transition marked in Fig. 11. When passing from $k = 1.45$ to $k = 1.46$ the main island ejects a resonance of smaller islands, therefore reducing the area of the main island. However, each ejected island has an elliptic periodic point in the middle, and by the Poincaré-Birkhoff theorem [39,40] there exists their corresponding hyperbolic fixed points pair. The action of the stable and unstable manifolds of these hyperbolic points is responsible for the changes in diffusion behavior since they provide large channels to escape from the main island [41–43].

Finally, considering an even more complicated mapping, the oval billiard, Eq. (15), we show similar results, see Fig. 13 and Fig. 14. Again, with these results we observe that changes of behavior in the diffusion exponent are related to changes in the area of the main island. In particular, we find that when the area of the main island is abruptly reduced, due the destruction of invariant tori and the creation of hyperbolic and elliptic fixed points, the diffusion exponent grows.

V. CONCLUSION

We showed that the use of Shannon entropy allows us to characterize the diffusion exponent in low-dimensional Hamiltonian systems described by maps. The method presented used the diffusion entropy analysis technique, where a relation between entropy and time exists, Eq. (16). To measure the entropy, we must construct a histogram where the number of bins is selected considering the diffusion range and the fluctuation size of the ensemble of trajectories, Eq. (18). The methodology proposed allowed us to calculate the diffusion exponent both in regions where the diffusion is normal, as in regions where the stickiness phenomenon is present, producing an anomalous diffusion.

We calculated the diffusion exponent for many values of the control parameter of the standard map and the oval billiard, where for each value the main island had a different shape, and then we showed that the changes of behavior in

the diffusion exponent were related with changes in the area of the main island. In particular, we found that when the main area of the main island is abruptly reduced, due the destruction of invariant tori and creation of hyperbolic and elliptic fixed points, the diffusion exponent grew. We believe this happened due the fact that the hyperbolic points reduced the stickiness by means of their unstable or stable manifold dynamics, since they provide *channels* to escape from the main island's shore.

ACKNOWLEDGMENTS

G.I.D. thanks the fellowship from National Council for Scientific and Technological Development (CNPq). M.S.P., I.L.C., and E.D.L. acknowledge Sao Paulo Research Foundation (FAPESP) Grants No. 2018/03000-5, No. 2018/03211-6, and No. 2017/14414-2. I.L.C. and E.D.L. acknowledge National Council for Scientific and Technological Development (CNPq) Grants No. 300632/2010-0 and No. 303707/2015-1.

[1] M. F. Shlesinger, G. M. Zaslasvsky, and J. Klafter, Strange kinetics, Nature **363**, 31 (1993).

[2] C. P. Dettmann, Diffusion in the Lorentz gas, Commun. Theor. Phys. **62**, 521 (2014).

[3] E. Fermi, On the origin of the cosmic radiation, Phys. Rev. **75**, 1169 (1949).

[4] A. J. Litchenberg, M. A. Lieberman, and R. H. Cohen, Fermi acceleration revisited, Physica D **1**, 291 (1980).

[5] S. O. Kamphorst, E. D. Leonel, and J. K. L. Da Silva, The presence and lack of Fermi acceleration in nonintegrable billiards, J. Phys. A **40**, F887 (2007).

[6] R. S. MacKay, J. D. Meiss, and I. C. Percival, Transport in Hamiltonian systems, Physica D **13**, 55 (1984).

[7] N. B. de Faria, D. S. Tavares, W. C. S. de Paula, E. D. Leonel, and D. G. Ladeira, Transport of chaotic trajectories from regions distant from or near to structures of regular motion of the Fermi-Ulam model, Phys. Rev. E **94**, 042208 (2016)

[8] D. F. Oliveira, M. R. Silva, and E. D. Leonel, A symmetry break in energy distribution and a biased random walk behavior causing unlimited diffusion in a two dimensional mapping, Physica A **436**, 909 (2015).

[9] A. L. P. Livorati, T. Kroetz, C. P. Dettmann, I. L. Caldas, and E. D. Leonel, Stickiness in a bouncer model: A slowing mechanism for Fermi acceleration, Phys. Rev. E **86**, 036203 (2012).

[10] G. M. Zaslasvsky, Chaos, fractional kinetics, and anomalous transport, Phys. Rep. **371**, 461 (2002).

[11] E. D. Leonel, J. A. De Oliveira, and F. Saif, Critical exponents for a transition from integrability to non-integrability via localization of invariant tori in the Hamiltonian system, J. Phys. A **44**, 302001 (2011).

[12] M. S. Palmero, G. I. Díaz, P. V. E. McClintock, and E. D. Leonel, Diffusion phenomena in a mixed phase space, arXiv:1907.11702.

[13] A. Bäcker, R. Ketzmerick, and S. Löck, Direct regular-to-chaotic tunneling rates using the fictitious-integrable-system approach, Phys. Rev. E **82**, 056208 (2010).

[14] C. Löbner, S. Löck, A. Bäcker, and R. Ketzmerick, Integrable approximation of regular islands: The iterative canonical transformation method, Phys. Rev. E **88**, 062901 (2013).

[15] A. N. Kolmogorov, On conservation of conditionally periodic motions for a small change in Hamilton's function, Dokl. Akad. Nauk SSSR. **98**, 527 (1954).

[16] J. Moser, On invariant curves of area-preserving mappings of an annulus, Nachr. Akad. Wiss. Göttingen II, 1 (1962).

[17] V. I. Arnold, Proof of a theorem of A. N. Kolmogorov on the preservation of conditionally periodic motions under a small perturbation of the Hamiltonian, Uspekhi Mat. Nauk **18**, (1963) (English transl., Russ. Math. Surv, vol. 18)

[18] N. Scafetta and P. Grigolini, Scaling detection in time series: Diffusion entropy analysis, Phys. Rev. E **66**, 036130 (2002).

[19] P. J. Morrison, Magnetic field lines, Hamiltonian dynamics, and nontwist systems, Phys. Plasmas **7**, 2279 (2000).

[20] D. del-Castillo-Negrete, Chaotic transport in zonal flows in analogous geophysical and plasma systems, Phys. Plasmas **7**, 1702 (2000).

[21] M. Roberto, E. C. Silva, I. L. Caldas, and R. L. Viana, Magnetic trapping caused by resonant perturbations in tokamaks with reversed magnetic shear, Phys. Plasmas **11**, 214 (2004).

[22] C. G. L. Martins, M. Roberto, and I. L. Caldas, Magnetic field line stickiness in tokamaks, IEEE Trans. Plasma Sci. **42**, 2764 (2014).

[23] G. Contopoulos, M. Harsoula, N. Voglis, and R. Dvorak, Destruction of islands of stability, J. Phys. A: Math. Gen. **32**, 5213 (1999).

[24] J. D. Meiss, Symplectic maps, variational principles, and transport, Rev. Mod. Phys. **64**, 795 (1992).

[25] I. C. Percival, A variational principle for invariant tori of fixed frequency, A variational principle for invariant tori of fixed frequency, J. Phys. A: Math. Gen. **12**, L57 (1979).

[26] A. J. Lichtenberg and M. A. Lieberman, *Regular and Chaotic Dynamics*, Applied Mathematical Sciences, Vol. 38 (Springer-Verlag, New York, 1992).

[27] B. V. Chirikov, *Research Concerning the Theory of Nonlinear Resonance and Stochasticity*, Preprint No. 267, Institute of Nuclear Physics, Novosibirsk, 1969 (Engl. Trans., CERN Trans. 71-40 1971).

[28] B. V. Chirikov, A universal instability of many-dimensional oscillator systems, Phys. Rep. **52**, 263 (1979).

[29] M. V. Berry, Regularity and chaos in classical mechanics, illustrated by three deformations of a circular billiard, Eur. J. Phys. **2**, 91 (1981).

[30] J. L. Lagrange, *Réflexions sur la résolution algébrique des équations* (CEuvres de Lagrange, III, Gauthier-Villars, 1869), pp. 205.

[31] J. Skowron and A. Gould, General complex polynomial root solver and its further optimization for binary microlenses, arXiv:1203.1034.

[32] G. D. Birkhoff, On the periodic motions of dynamical systems, Acta Math. **50**, 359 (1927).

[33] NIST DLMF, Digital Library of Mathematical Functions, edited by W. J. Olver, A. B. Olde Daalhuis, D. W. Lozier, B. I. Schneider, R. F. Boisvert, C. W. Clark, B. R. Miller, and B. V. Saunders (2019).

[34] F. T. Krogh, C. L. Lawson, and W. Van Snyder (eds.), MATH77 and mathc90, release 6.0. Libraries of Mathematical Subprograms in Fortran 77 and C, California Institute of Technology, 1998.

[35] C. E. Shannon, A mathematical theory of communication, Bell Syst. Tech. J. **27**, 379 (1948).

[36] We use the convention $0 \ln(0) = 0$.

[37] We know that we always will be able to find it since the minimal of all q_0 is quasiperiodic and also q_f marks a yellow box, i.e., chaotic region.

[38] P. Dierckx, *Curve and Surface Fitting with Splines* (Oxford University Press, Oxford, 1995).

[39] S. Lange, M. Richter, F. Onken, A. Bäcker, and R. Ketzmerick, Global structure of regular tori in a generic 4D symplectic map, Chaos **24**, 024409 (2014).

[40] G. D. Birkhoff, An extension of Poincaré's last geometric theorem, Acta. Math. **47**, 297 (1926).

[41] Y. S. Sun, L. Zhou, and J. L. Zhou, The role of hyperbolic invariant sets in stickiness effects, in *A Comparison of the Dynamical Evolution of Planetary Systems* (Springer, Dordrecht, 2005).

[42] T. S. Kruger, P. P. Galuzio, T. L. Prado, R. L. Viana, J. D. Szezech, and S. R. Lopes, Mechanism for stickiness suppression during extreme events in Hamiltonian systems, Phys. Rev. E **91**, 062903 (2015).

[43] G. Contopoulos and M. Harsoula, Stickiness effects in chaos, Celest. Mech. Dynam. Astron. **107**, 77 (2010).